

Research Type (Original Article)

Unsteady Surface Pressure Characterization of the Base Pressure Region of a Heavy Goods Vehicle

Author: Alvin Gatto*

Details:

First Name: Alvin

Last Name: Gatto

Affiliation: Brunel University London, Uxbridge, Middlesex, UB8 3PH

Email Id: alvin.gatto@brunel.ac.uk

ORCID Id: <https://orcid.org/0000-0003-4443-0451>

Abstract

This paper presents an experimental investigation into the time-dependent aerodynamics within the base region of a representative heavy goods vehicle. The work conducted is surface-based, and involved using multiple, customized dynamic pressure sensors for both aligned and mis-aligned flow configurations. Uniquely, the methodology adopted allowed high resolution, detailed interrogation of this region and the presentation of several new insights. Among the most significant are the detailed characterization and quantification of the degree of flow-misalignment necessary to prompt development of a complex vortex/wake structure reported previously. Once developed, this structure dominated the upper-windward quadrant of the base region with measured unsteady surface loads up to 2-3 times greater than that observed under nominal flow conditions. Presented spectral information also showed evidence of both Strouhal-based vortex shedding within the wider base-pressure region as well as more localized regions containing higher spectral contributions centered broadly at several multiples of the primary shedding frequency.

Keywords:

Heavy goods vehicles; Unsteady surface pressure; Road vehicle drag

1. INTRODUCTION

As the need to move goods around the globe increases in both volume and frequency, increasing attention is now focused on the impact these activities have on our planet through harmful carbon dioxide emissions[1]. Road transport is a significant contributor to this environmental problem with one-quarter of all transport emissions resulting from the use of Heavy Goods Vehicles(HGV)[1]. Looking to the future, further in-depth understanding of the flow-field around these vehicles remains paramount if new innovative ways to limit these emissions are to be developed.

At highway speeds, HGVs use approximately half of the useable engine power to overcome aerodynamic drag[2-3]. Categorized as a bluff body, more than 90% of the aerodynamic drag is pressure drag[4-5] where large differential pressures are setup between the forward and rearward faces of the vehicle. Over the last few decades, many different passive and active techniques have

been investigated to reduce drag. Boat-tails[2-3,6-9], rear cavities[10-11], skirts[2, 6-7,12], roof deflectors[6], tractor-trailer gap treatments[2], vortex generators[2,13-14], suction/bleed/blowing/ventilation systems[13-15], and extension panels[2,6] have all been investigated, however, principally from a time-independent perspective[16]. The time-dependent nature of the flow, particularly under mis-aligned flow conditions, remains critically underexplored. As these vehicles operate in a dynamic environment where off-axis wind, atmospheric boundary layers, gusts, upstream interference and turbulence in traffic all effect the vehicle's aerodynamic performance, stability, and fuel consumption[3,5,16-17], a knowledge deficiency currently exists of how many of these influences affect the vehicle. These influences are expected to have significant implications on the vehicle flowfield, with boundary layer development, separation patterns, fuel consumption, and overall stability, being adversely affected[5,11]. More information such as maximum peak and unsteady root mean square (RMS) pressures, forces, and moments, wake shedding frequencies as well as detailed characterization of unsteady wake regions would all aid greater understanding and contribute further to lower drag vehicles with enhanced inherent stability.

The current study seeks to build on existing work[2,13,17,22], in the characterization of the time-dependent flow dynamics that exist during representative HGV operational conditions. Predominantly, results presented here detail mean, unsteady, and spectral surface pressure information within the base pressure region for both aligned and mis-aligned flow conditions. Where possible, connections are also made to the off-surface wake flow as well as probable implications for vehicle drag and stability.



Fig. 1. Wind tunnel test setup with instrument base, $Re_n = 8 \times 10^5$.

2. MATERIALS AND METHODS

The model used for all testing is shown in Fig. 1. Based on a full-scale vehicle utilized by a large supermarket chain, the 1:10th scale tractor and trailer sections were installed on a fixed ground plane with both a vertical strut (extending through the ground plane), and sliding wheel contacts used to locate the model. Constructed from a combination of 3D printed, machined, and hand-finished components, the model measured 1.62m in length, 0.26m in width, and 0.4m in height. For the trailer element, the design incorporated a large evacuated internal volume as well as a reconfigurable rear section (0.2m in length) to allow aerodynamic testing of different base configurations (Fig. 1). For the current investigation, a standard, unmodified, base was used. Within the internal volume of the trailer, a wireless data acquisition system together with a combination of 27 individual pressure

sensors was used to measure surface pressure data. A total of 105 different sensor locations around the top, bottom, back, and sides of the rear insert were possible(Fig. 2). At each of these locations, an 0.8mm diameter surface tap located the measurement position with each sensor diaphragm located approximately 4mm behind the surface tapping position. No transmission corrections were used.

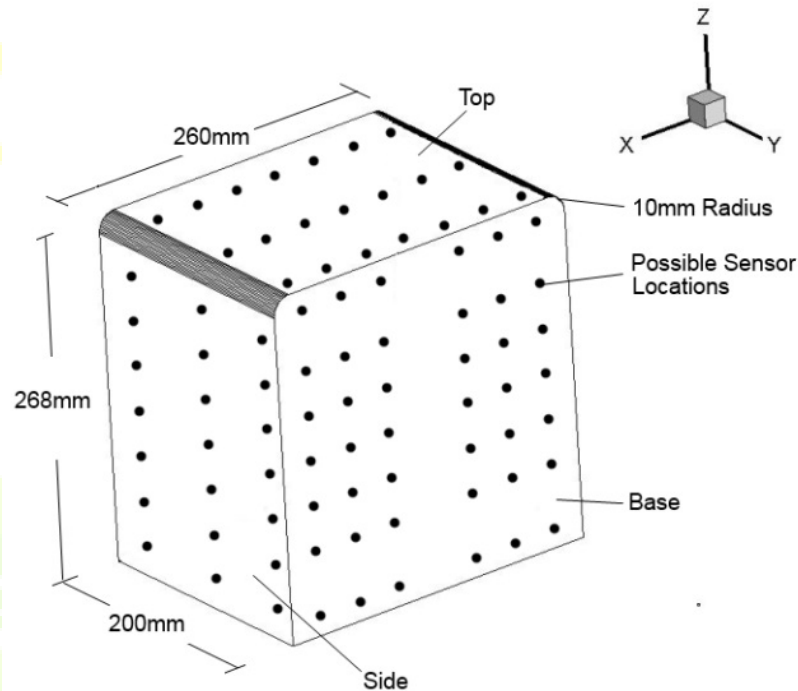


Fig. 2. Detail of sensor locations for the instrumented base(to scale).

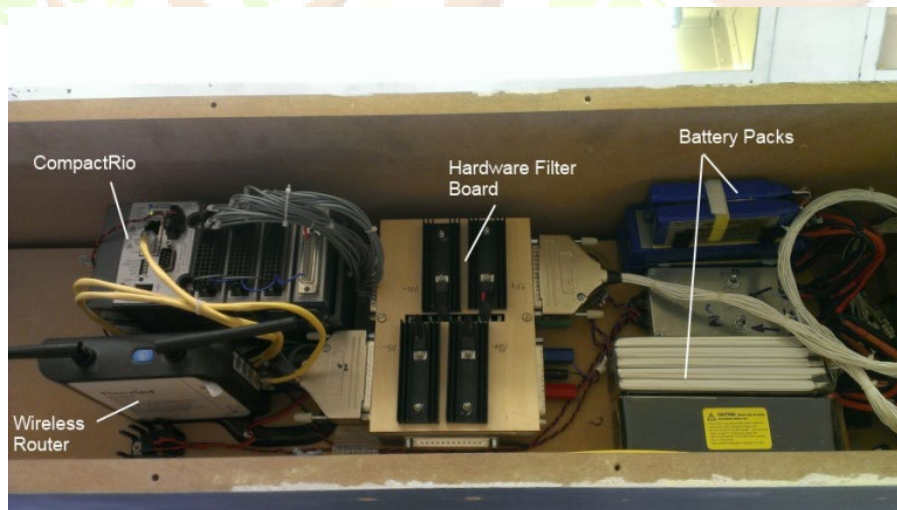


Fig. 3. Wireless data acquisition setup installed inside the trailer internal volume.

Honeywell CPC03GFH pressure transducers were used for all measurements. These active strain-gauge/diaphragm sensors have a cylindrical measurement port and connections for PCB mounting.

A custom-designed miniature PCB was integrated onto each transducer to provide signal amplification and conditioning capabilities. Overall, these devices measured $20 \times 10 \times 7$ mm, were in-expensive, with flat frequency response characteristics over the frequency range of interest to this study (2.5kHz). More information on the sensors used, including nominal calibration and frequency response characteristics, can be found in [18].

For this investigation, a custom wireless data acquisition system (Fig. 3) was configured and installed inside the evacuated trailer volume. A CompactRIO 9025, running multiple NI9025, 16-bit, Analog Input modules, was used as the primary data acquisition hardware. Custom-programmed FPGA control architecture linked through a wireless router to an external laptop positioned outside the wind tunnel coordinated the data acquisition process. Prior to data acquisition at 10kHz, each individual pressure signal was amplified and subsequently filtered via 8th-order elliptical, low-pass, integrated circuits (cut-off frequency set to 3.5kHz). A single TTL timing signal from a NI9264 module operating at 350kHz controlled this operation. All data was sampled for 10 seconds giving 100 000 samples for subsequent post-processing.

To monitor the internal static pressure within the model during wind tunnel testing, another pressure sensor was installed inside the instrumented base. This sensor was mounted at the mid-volume internal position with the reference port exposed, via plastic tubing, to the outside environment of the wind tunnel. This sensor information was monitored as all surface pressure data needed to be referenced, and therefore corrected, to the wind tunnel static pressure. Although varying in mean value with increasing flow mis-alignment, internal static pressure data was found to be essentially time-invariant during the data sampling interval. All data was subsequently corrected for these mean pressure changes.

To obtain a complete surface pressure map of the instrumented base, multiple wind tunnel test runs, with manual repositioning of the sensor bunch, was used. In total, three separate sensor distributions, covering predominantly the side, top, and back, were tested. The 'side' configuration utilised all 21 sensors on the side face (Fig. 2) as well as the three nearest top (shown) and bottom sensors (not shown). The 'top' distribution used all top surface taps together with the nearest three sensors on both sides of the base. Lastly, the 'back' distribution used all 21 sensors on the left side of the back face as well as mid-height sensors on the sides and mid-width sensors on the top and bottom. When not in use, vacant sensor locations were sealed with adhesive tape to isolate external pressures from the internal cavity.

The model was tested in a closed-circuit wind tunnel with a maximum flow velocity of 60 m/s and a closed test section measuring 1.68×1.22 m. The minimum model blockage, based on frontal area at zero yaw, was 5.5% (no corrections applied). The turbulence intensity at model station was 0.2% with the operating flow speed for this investigation set at 45 m/s. These test conditions gave a Reynolds number, based on model width, of $Re_n = 8 \times 10^5$ exceeding the recommendations of both [19] and [20].

Before and after every test run, a zero, wind-off, data point was taken. This allowed compensation for any thermal drift of measurement zeros during the experiments as well as identification of superfluous, non-aerodynamic, frequency components in the data collected. For each of the test runs completed, a yaw angle sweep from $\psi = 0^\circ$ to $\psi = 10.5^\circ$, to $\psi = -10.5^\circ$, and back to $\psi = 0^\circ$ (step of $\psi = 3.5^\circ$) was adopted. Data taken at the same yaw angle and pressure tapping location was averaged with model flow symmetry assumed for the case of zero yaw. Results taken at non-zero yaw angle were decomposed and presented based on exposure to either the windward or leeward sides of the model. For example, 'side' data taken at $\psi = 10.5^\circ$ representing sensor windward flow exposure was

coupled with data at $\psi = -10.5^\circ$ representing leeward exposure to complete the $\psi = 10.5^\circ$ results (Fig. 3). This methodology, also adopted for both the 'top' and 'back' sensors distributions, allowed effective and time-efficient use of one complete yaw sweep to map the resulting surface pressures.

3. RESULTS AND DISCUSSIONS

Contour plots of C_p obtained from linear interpolation of the sensor data are presented in Fig. 3. Considering the transition from $\psi = 0^\circ$ to $\psi = 3.5^\circ$ initially, only subtle topological changes were observed ($\Delta C_p \leq \approx 10\%$). At both $\psi = 0^\circ$ to $\psi = 3.5^\circ$, results show the lower half of the base region encompassing a large area of low pressure whose magnitude is approximately twice that observed for the upper half [17]. This topology has been reported previously and results from the formation of a recirculating wake precipitated by differential wake velocities (over the top and bottom the vehicle) [8]. This feature remains evident across the majority of the base width with the lowest pressures measured at $C_p \approx -0.31$ (mid-width). From top and side perspectives, results also show only marginal variations ($\Delta C_p \leq \approx 10\%$) indicating, at least for $0^\circ < \psi < 3.5^\circ$, relatively benign deviations exist for C_p within this region.

With additional increases to $\psi = 7^\circ$ and $\psi = 10.5^\circ$ (Fig. 3c-d), topology changes become more distinct. Comparing Figs. 3c to 3b, substantial wake asymmetry has developed with lower pressures concentrated ($C_p = -0.40$) within the bottom leeward quadrant of the base. Considering the size and magnitude of the low pressures within this area, targeting and placating these pressures should be one aim of any base pressure drag reduction technique. Segregating this region with the upper windward sector of the base, a distinct surface pressure discontinuity exists. Similar results are shown in [2]. Almost curvilinear in nature, this boundary defines the extent of a rear-wake vortical structure created from flow separation over the upper windward edge of the trailer side [9,21]. As is shown in Fig. 3d, the surface footprint of this feature is substantial, subtending past both the mid-width and mid-height locations. While high however, pressure within this regions was found to be higher ($C_p \approx -0.27$) and more moderate than those observed at the bottom leeward quadrant with only marginal increases found over those observed at $\psi = 0^\circ$ ($C_p \approx -0.23$). These trends agree with data from [22].

A similar, almost discrete topological change, is also evident from the top perspective. From these results, the same developed vortex indicates a near constant-width surface footprint of lower pressure ($C_p \approx -0.35$) extending to base mid-width. Results from previous work [8,21-23] have also characterised this feature on the top of the vehicle with qualitative agreement in size to results presented here. Distinct from the surface footprint on the back surface however, results from the top indicate initial upper edge flow separation together with subsequent flow re-attachment (recovery to higher pressure magnitudes).

ग्रन्थालयाः

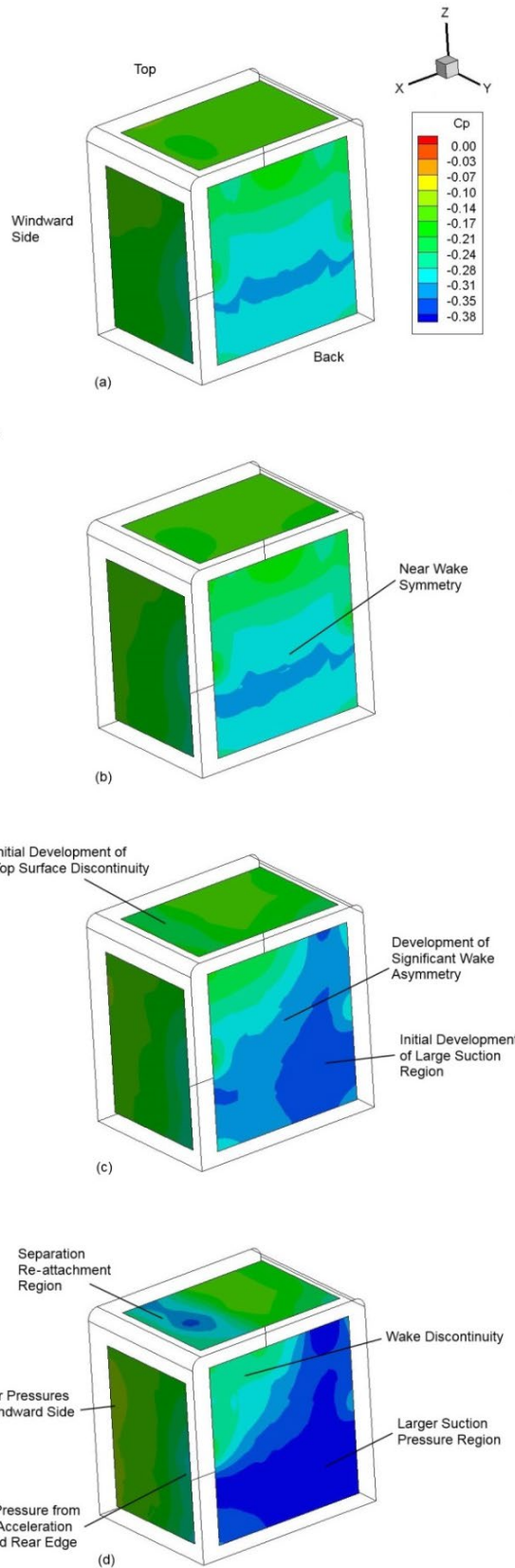


Fig. 3. Mean C_p distributions obtained from the instrumented base; (a) $\psi = 0^\circ$, (b) $\psi = 3.5^\circ$, (c) $\psi = 7^\circ$, (d) $\psi = 10.5^\circ$.

Another well-known implication of increasing flow mis-alignment is the differential pressures setup between the windward and leeward sides of the model[21-22]. This is most notable considering Fig. 3d with maximum side $C_p \approx -0.12$ (windward) compared to $C_p \approx -0.24$ (leeward not shown) at the same positions($C_p \approx -0.15$ at $\psi = 0^\circ$). Averaging the results on either side, pressure was found to 30% lower in magnitude on the leeward side compared to the windward. While this consequence of applied yaw is somewhat obvious as the windward side is exposed to more direct airflow, results also show additional, more subtle features. One such feature is the decrease in pressure at the rear windward back edge as the flow accelerates into the wake[2,21]. As would be expected this region is somewhat localized subtending upstream only one quarter of the vehicle width, however, within this region, surface pressure was found to be significant ($C_p \approx -0.29$) at more than double that observed further upstream($C_p \approx -0.13$). Although not considered a direct contributor to drag, this low pressure region preempts the degree of flow curvature to the wake, and therefore, continues to hold possibilities for subsequent wake size manipulation via artificial enhancement.

Less frequently considered in the published literature, and presented in Fig. 4, the C_{prms} data provides additional insights into the flow physics that may not otherwise be possible with consideration of C_p only. Directly comparable to flow conditions from Fig. 3, these results show increased flow unsteadiness within the vortex surface footprint discussed earlier for C_p . Reaching maximum magnitudes at the highest levels of flow mis-alignment(Fig. 4d), results within these areas were found to be more than two and a half times that observed for aligned flow conditions. The maximum C_{prms} was measured at $C_{prms} = 0.044$ (upstream windward region on the top surface). Together with being an area of elevated flow unsteadiness, interrogation of the data also showed near magnitude consistency within the regions affected($C_{prms} \approx 0.03-0.04$). These included both the upper windward quadrant of the back face as well as the windward side of the top surface. Noting the magnitude, surface footprint area, and asymmetric nature of this unsteady loading, it is considered likely that existence of this flow feature would contribute somewhat to reducing inherent vehicle stability.

Co-incident with the results already discussed for C_p , initial signs of the development of the vortex feature are also shown in the C_{prms} data between $\psi = 3.5^\circ$ to $\psi = 7^\circ$ (Figs. 4b-c). For $\psi = 0^\circ$, the unsteady surface loading appears to be characterised by relative flow stability ($C_{prms} \approx 0.01-0.015$), particularly on faces oriented perpendicular to the flow direction. As would be expected, the back face was found to be the exception with upper half unsteady magnitudes ($C_{prms} \approx 0.026$) being more than 50% greater than the lower half ($C_{prms} \approx 0.017$). This result is consistent with the formation of the two-vortex wake system mentioned earlier with higher incident flow velocities over the top mixing within the low velocity wake[8]. Similar results were also found for $\psi = 3.5^\circ$, and while initial signs of flow asymmetry on the back face are evident (C_{prms} reduces in the leeward upper quadrant), C_{prms} magnitudes were found to be relatively invariant compared those observed at $\psi = 0^\circ$ ($\Delta C_{prms} < 10\%$). Only with further changes in flow mis-alignment ($\psi \geq 7^\circ$) do clear indications of both increases in C_{prms} magnitude as well as a defined segregating surface pressure boundary exist. These are most evident for the upper windward areas of the back and top faces (Figs. 4c-d).

ग्रन्थालयाः

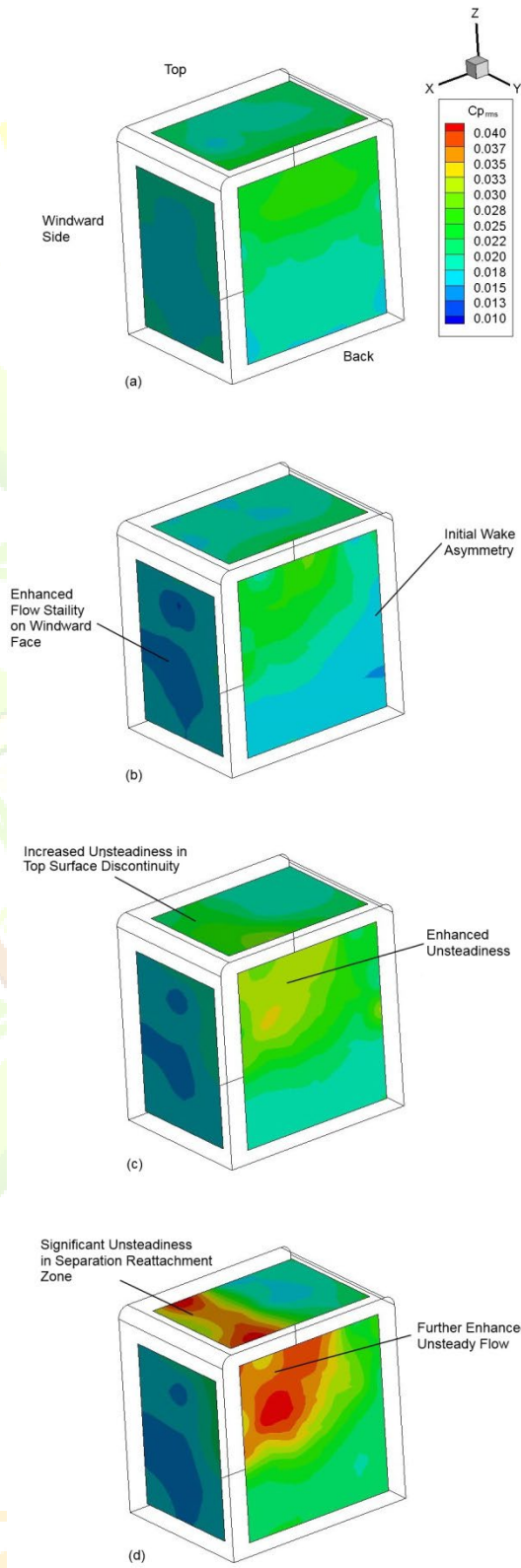


Fig. 4. C_{prms} distributions obtained from the instrumented base; (a) $\psi = 0^\circ$, (b) $\psi = 3.5^\circ$, (c) $\psi = 7^\circ$, (d) $\psi = 10.5^\circ$.

In a similar manner to that already described for C_p , C_{prms} magnitudes also show significant differences between the leeward and windward sides of the base under mis-aligned flow conditions. At its largest for $\psi = 10.5^\circ$, averaged leeward side C_{prms} was found to be up to 60% greater ($C_{prms} \approx 0.0175$ at $\psi = 0^\circ$), than that observed on the windward. Most of this contribution ($\approx 50\%$) exists due to an almost consistent increase in flow instability on the leeward face of the base (averaged $C_{prms} \approx 0.0265$) however, there is also evident a small contribution ($\approx 10\%$) resulting from an increase in flow stability on the windward face ($C_{prms} \approx 0.0165$). Although these average values are somewhat lower than those measured for the vortex feature discussed earlier, these differential unsteady magnitudes act over much larger surface areas (trailer sides), and as such, would also be expected to adversely affect overall vehicle stability.

One of the main advantages of including individual spectral data is that further detail of flow behavior, not readily available within the results already discussed, can be obtained. To provide some of these additional insights, pressure spectra comparing $\psi = 0^\circ$ to $\psi = 10.5^\circ$ within the Strouhal number range from $0 < St < 3$ are presented (Figs. 5-6). All spectra (dB re 1Pa) were obtained from averaging 19 individual time segments (0.5s duration) using a Hanning window with 50% overlap.

Considering Fig. 5 initially, for the case of $\psi = 0^\circ$ (black lines), two distinct peaks are shown. The first peak, much more subtle than the second, is predominantly observed on each of the sides of the base and centred at $St \approx 0.11$ (Fig. 5d). Expected to represent traditional wake vortex shedding [2,17] from the model ($St \approx 0.14$ from [2], $St \approx 0.12$ from [24]), these peaks were not representative of a large intensity, dominating wake oscillatory frequency, but a relatively benign oscillation integrated within more broader-based, lower frequency, flow energies [17,24]. Evident over most of the base height at all streamwise measurement locations for the sides (Upstream, Middle, and Rear), top and back (Fig. 6) surface data appeared devoid of this peak. This result was thought to be due to the increased wake flow energies evident on the back face (≈ 10 dB) relative to the sides (≈ 5 dB) for $\psi = 0^\circ$ (at $St \approx 0.11$) as well as the relative isolation of the top sensor positions to this predominantly transverse flow oscillation. It appears likely that the detection of this first, subtle oscillatory peak, is best accomplished by sensors placed near directly affected edges.

The second distinct peak identifiable in the spectra for $\psi = 0^\circ$ was centred at $St \approx 0.62$ (Fig. 5d). Possessing lower inherent energy (0.62dB) than the peak at $St \approx 0.11$ (6.3dB, 1WU), this peak appears much broader in bandwidth and remains relatively consistent in magnitude and frequency for both the $\psi = 0^\circ$ and $\psi = 10.5^\circ$ flow cases (including all top, side, and back faces). Analysis of the spectral information from the reference sensor mounted inside the instrumented base also showed evidence of this peak (not presented). This consistency, together with the detection of this peak inside the trailer volume suggests a non-aerodynamic related source (structural) although additional investigations are needed in order to fully understand the primary cause of this oscillation.

Comparing directly spectral data obtained at $\psi = 0^\circ$ and $\psi = 10.5^\circ$, several distinct flow features are present. For the top surface of the base (Figs. 5a-c), all three subfigures indicate broad regions of increased spectral energy coincident within the most windward measurement positions (5TR-7TR, 5TM-7TM, 5TU-7TU). Centered at increasing Strouhal numbers with movement towards the base mid-width ($1 < St < 1.6$), these results coincide with regions already identified as the surface footprint of a developed vortex. Initiated from the upper windward edge of the base, results identify the increase in flow energies at higher frequencies typical of regions of flow separation, as

well as the return of spectral topology (almost identical to $\psi = 0^\circ$) indicative of subsequent flow reattachment (1TR-3TR). Interestingly, results for the most rearward position on the top surface (Fig. 5c) also show the presence of a set of strong spectral peaks (max $\approx 15\text{dB}$) centered at $St \approx 0.18$ for $\psi = 10.5^\circ$ (5TR-7TR). It appears that these peaks, which reduce in intensity with movement to mid-width, characterise a fundamental oscillatory frequency within the vortex-wake feature described earlier in Figs. 4c-d. Nothing that Figs. 5a-b show no evidence of such peaks at this Strouhal number, this behaviour appears unrelated to the fundamental development of the vortex region on the top surface, but due to the localised unsteady region defined within the upper windward base wake area. This assertion is further supported by considering data presented in Fig. 6(a,c,e). With similar peaks also shown in these subfigures(1WO-3WO, 2WC-4WC, 2WI-5WI), it appears likely that the top sensors have detected this oscillatory wake frequency rather than being directly within its influence. Devoid at $\psi = 0^\circ$, these peaks were found to develop with increasing intensity and Strouhal number as flow misalignment increased (16dB at $St \approx 0.14$ for $\psi = 7^\circ$, 20dB at $St \approx 0.18$ for $\psi = 10.5^\circ$, 3WC). At some the highest magnitudes measured in any of the test configurations conducted, these results further support the assertion that this region is likely one of the main areas contributing to impairing inherent vehicle stability under mis-aligned flow conditions.

Another flow characteristic observed within the spectral data expected to degrade vehicle stability is evident when comparing Figs. 5d,f,h to Figs. 5e,g,i. Representing windward and leeward side data respectively, spectral topologies between the two sides are fundamentally different. Results for the windward spectra indicate a near-constant reduction ($<10\text{dB}$) in flow energies for $St < 0.6$ (Figs. 5d,f) compared to $\psi = 0^\circ$. As discussed in previous sections, results on the windward face of the base undergo an increase in flow stability as more favourable pressure gradients exist. Only apparent from interrogation of the spectral data however, this flow stability mechanism appears predominantly manifested within the lower frequency ranges($St < 0.6$). One exception to this effect occurs at the most rearward positions on the windward side (Fig. 5h). Comparing this data to Figs. 5d,f, an increase in flow instability to levels more akin to conditions at $\psi = 0^\circ$ is observed. These results agree with both the lower pressures (C_p) and reduced flow stability (C_{prms}) characteristics discussed earlier at these positions as the flow pre-empts integration into the base wake.

For the leeward side(Fig. 5e,g,i), spectral topologies indicate a significant increase in broadband flow energy at all Strouhal numbers presented. Characteristic of this side of the base, spectral magnitudes also possess a near consistency independent of either the height of the base or stream-wise position. Comparing these results to $\psi = 0^\circ$, a near 10-15 dB magnitude increase exists for $St > 1$, with this increase predominantly observed at lower measurement positions(3LU-7LU, 3LM-7LM, 3LR-7LR). For $\psi = 10.5^\circ$, leeside results also appear devoid of any dominant oscillatory spectral peaks, indicating instead, a much broader-based oscillatory flow instability. If, as expected, these characteristics exist over the significant portion of the leeside area of the trailer, this region would also be expected (perhaps the most dominant) to reduce the stability of the complete vehicle under mis-aligned flow conditions.

ग्रन्थालयाः

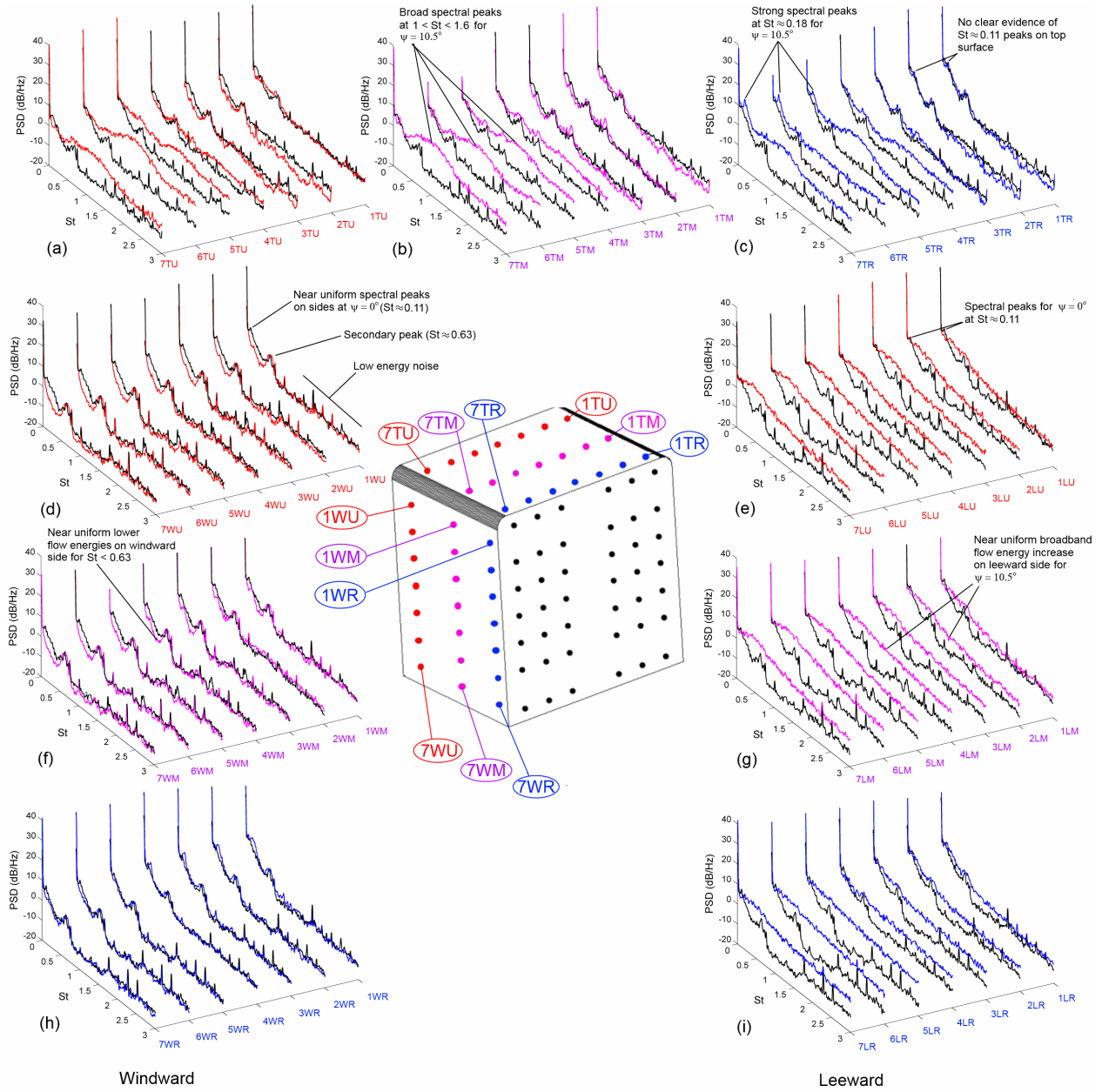


Fig. 5. Frequency spectra obtained from the sides and top of the instrumented base at $\psi = 10.5^\circ$ (colored) compared to $\psi = 0^\circ$ (black).

शान्तालयाः

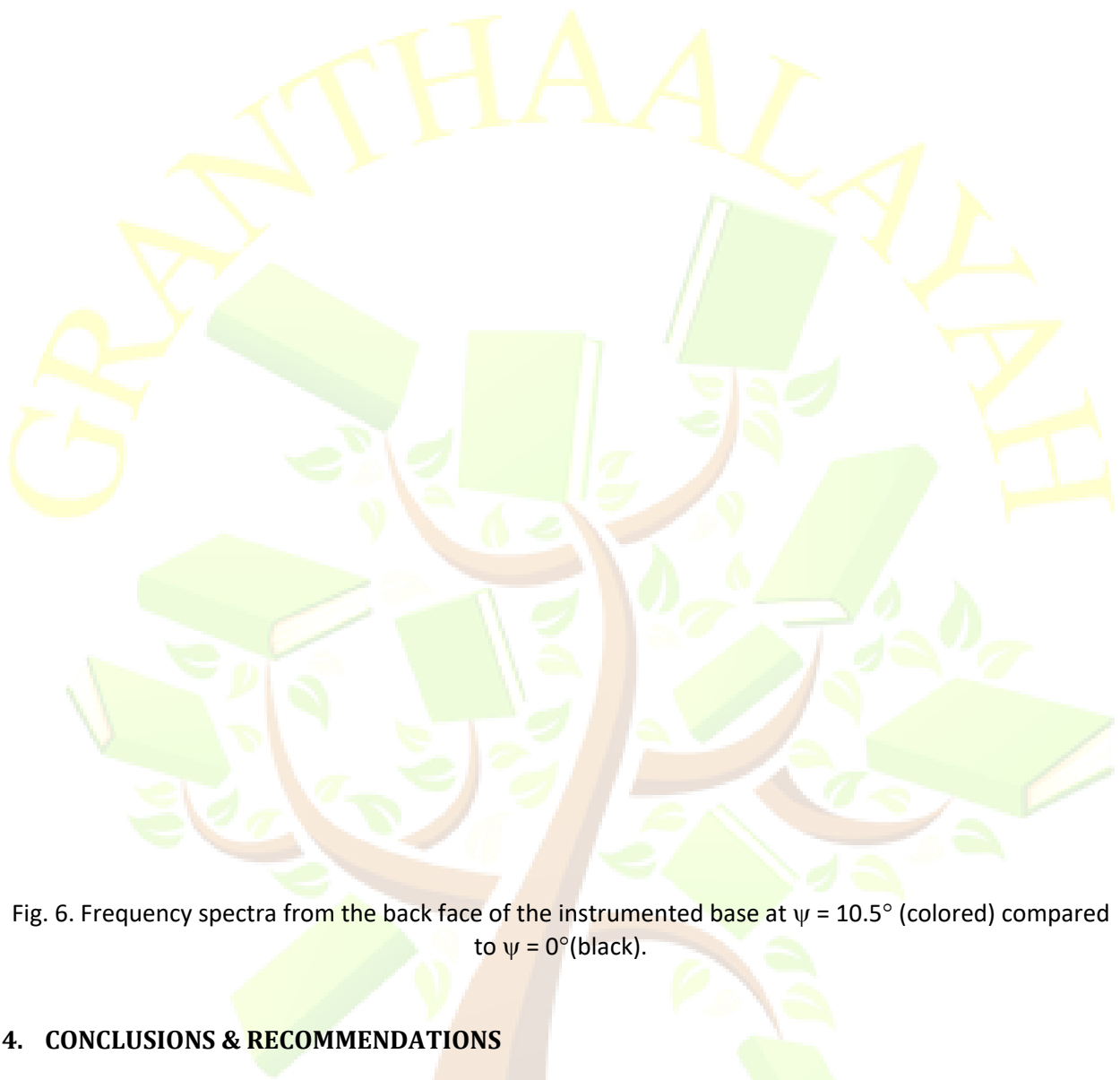


Fig. 6. Frequency spectra from the back face of the instrumented base at $\psi = 10.5^\circ$ (colored) compared to $\psi = 0^\circ$ (black).

4. CONCLUSIONS & RECOMMENDATIONS

This paper has detailed an experimental investigation into the time-dependent surface pressure aerodynamics within the base region of a representative heavy goods vehicle. The 1:10th scale model utilized multiple arrays of custom-configured miniature pressure sensors together with an integrated wireless data acquisition system to obtain detailed mean and unsteady pressure data. Results included both aligned and mis-aligned flow conditions. Among the principal findings of the work was the interrogation of a vortical structure initially detected between 3.5 to 7 degrees of flow mis-alignment that produced significant unsteady surface loading over the windward top, as well as upper windward back faces of the base. These regions also incurred either locally, or in close proximity, low pressure that need to be placated if drag reduction is sought. Individual spectral data also identified several flow characteristics including regions of flow separation and reattachment over the top windward surface, as well as dominant oscillatory peaks within a vortex-wake combination located in the upper windward quadrant of the back face. As well as quantifying the size, characteristics, and nature of the main energy containing flow structures, it is hoped that this


information will lead to more effective development, as well as better optimization, of current and future drag reduction and vehicle stability technologies.

5. ACKNOWLEDGEMENTS

The author acknowledges the invaluable assistance and support provided academic and technical staff of Cambridge University.

REFERENCES

- [1] HM Government, "The Carbon Plan: Delivering our Low Carbon Future," Department of Energy & Climate Change, UK Government, December 2011.
- [2] Storms, B. L., Satran, D. R., Heineck, J. T., and Walker, S. M., "A Summary of the Experimental Results for a Generic Tractor-Trailer in the Ames Research Center 7- by 10-Foot and 12-Foot Wind Tunnels," NASA/TM-2006-213489.
- [3] Belzile, M., "Review of Aerodynamic Drag Reduction Devices for Heavy Trucks and Buses," CSTT-HVC-TR-205.
- [4] Ekman, P., Gårdhagen, R., Virdung, T., and Karlsson, M., "Aerodynamic Drag Reduction - from Conceptual Design on a Simplified Generic Model to Full-Scale Road Tests," SAE Technical Paper 2015-01-1543, 2015, doi:10.4271/2015-01-1543.
- [5] Wood, R., "Reynolds Number Impact on Commercial Vehicle Aerodynamics and Performance," SAE Int. J. Commer. Veh. 8(2):2015, doi:10.4271/2015-01-2859.
- [6] Burton, D., McArthur, D., Sheridan, J., and Thompson, M., "Contribution of Add-On Components to the Aerodynamic Drag of a Cab-Over Truck-Trailer Combination Vehicle," SAE Int. J. Commer. Veh. 6(2):2013, doi: 10.4271/2013-01-2428.
- [7] Waltzer, S., Hawkins, J., Mitcham, A., Lock, A. et al., "Wind Tunnel Evaluation of Potential Aerodynamic Drag Reductions from Trailer Aerodynamic Component Combinations," SAE Technical Paper 2015-01-2884, 2015, doi:10.4271/2015-01- 2884.
- [8] Salati, L., Cheli, F., and Schito, P., "Heavy Truck Drag Reduction Obtained from Devices Installed on the Trailer," SAE Int. J. Commer. Veh. 8(2):2015, doi:10.4271/2015-01-2898.
- [9] McCallen, R., Flowers, D., Dunn, T., Owens, J. et al., "Aerodynamic Drag of Heavy Vehicles (Class 7-8): Simulation and Benchmarking," SAE Technical paper 2000-01-2209
- [10] Kehs, J., Visser, K., Grossman, J., Niemiec, J. et al., "A Comparison of Full Scale Aft Cavity Drag Reduction Concepts With Equivalent Wind Tunnel Test Results," SAE Int. J. Commer. Veh. 6(2):2013, doi:10.4271/2013-01-2429.
- [11] Duell, E. G., and George, A. R., "Experimental Study of a Ground Vehicle Body Unsteady Near Wake," SAE Technical paper 1999-01-0812.
- [12] Eagles, N. and Cragun, M., "A Parametric Assessment of Skirt Performance on a Single Bogie Commercial Vehicle," SAE Int. J. Commer. Veh. 6(2):2013, doi:10.4271/2013-01-2415.
- [13] Hoffmann, F., Schmidt, H., Nayeri, C., and Paschereit, O., "Drag Reduction using Base Flaps Combined with Vortex Generators and Fluidic Oscillators on a Bluff Body," SAE Int. J. Commer. Veh. 8(2):2015, doi:10.4271/2015-01-2890.
- [14] Ortega, J., Salari, K., and Storms, B., "Investigation of Tractor Base Bleeding for Heavy Vehicle Aerodynamic Drag Reduction," UCRL-PROC-235892.
- [15] Englar, R. J. Improved Pneumatic Aerodynamics for Drag Reduction, Fuel Economy, Safety and Stability Increase for Heavy Vehicles, SAE Technical Paper, 2015, 2005-01-3627

- 
- [16] Gaylard, A., Oettle, N., Gargoloff, J., and Duncan, B., "Evaluation of Non-Uniform Upstream Flow Effects on Vehicle Aerodynamics," SAE Int. J. Passeng. Cars - Mech. Syst. 7(2):2014, doi:10.4271/2014-01-0614.
- [17] Horrigan, K., Duncan, B., Keating, A., Gupta, A. et al, "Aerodynamic Simulations of a Generic Tractor-Trailer: Validation and Analysis of Unsteady Aerodynamics," SAE Technical paper 2008-01-2612.
- [18] Gatto, A. & Graham, W. R., Investigation of Unsteady Surface Pressures over a Two-Wheeled Landing-Gear Model, AIAA Journal of Aircraft, August 2016, DOI: 10.2514/1.C033815
- [19] Watkins S., "Wind-Tunnel Modelling of Vehicle Aerodynamics: With Emphasis on Turbulent Wind Effects on Commercial Vehicle Drag", Thesis, Victorian University of Technology, 1990.
- [20] SAE Recommended Practice, "SAE Wind Tunnel Test Procedure for Trucks and Buses", SAE J1252, 1979.
- [21] Croll, R. H., Gutierrez, W. T., Hassan, B., Suazo, J. E., and Riggins, A. J., "Experimental Investigation of the Ground Transportation Systems (GTS) Project for Heavy Vehicle Drag Reduction," SAE paper 960907, 1996.
- [22] Storms, B. L., Ross, J. C., Heineck, J. T. et al, "An Experimental Study of the Ground Transportation System (GTS) Model in the NASA Ames 7- by 10-Foot Wind Tunnel." NASA/TM-2001-209621, February, 2001.
- [23] McCallen, R., Couch, R., Hsu, J., Browand, F. et al., "Progress in Reducing Aerodynamic Drag for Higher Efficiency of Heavy Duty Trucks (Class 7-8)," SAE Technical Paper 1999-01-2238, 1999, doi:10.4271/1999-01-2238.
- [24] Lanser, W., Ross, J., and Kaufman, A., "Aerodynamic Performance of a Drag Reduction Device on a Full-Scale Tractor/Trailer," SAE Technical Paper 912125, 1991, doi:10.4271/912125.
- ग्रन्थालयाः